Silicon strip detector for a novel 2D dosimetric method for radiotherapy treatment verification

A. Bocci [a,*], M.A. Cortés-Giraldo [b], M.I. Gallardo [b], J.M. Espino [b], R. Arráns [c], M.A.G. Alvarez [a,b], Z. Abou-Haïdar [a], J.M. Quesada [b], A. Pérez Vega-Leal [d], F.J. Pérez Nieto [e]

[a] National Accelerator Centre (CNA), 41092 Seville, Spain
[b] Department of Atomic, Molecular and Nuclear Physics (FAMN), University of Seville, 41012 Seville, Spain
[c] Virgen Macarena University Hospital, 41009 Seville, Spain
[d] School of Engineering, University of Seville, 41092 Seville, Spain
[e] Instalaciones Inabensa S.A., 41007 Seville, Spain

ARTICLE INFO

ABSTRACT

The aim of this work is to characterize a silicon strip detector and its associated data acquisition system, based on discrete electronics, to obtain in a near future absorbed dose maps in axial planes for complex radiotherapy treatments, using a novel technique. The experimental setup is based on two phantom prototypes: the first one is a polyethylene slab phantom used to characterize the detector in terms of linearity, percent depth dose, reproducibility, uniformity and penumbra. The second one is a cylindrical phantom, specifically designed and built to recreate conditions close to those normally found in clinical environments, for treatment planning assessment. This system has been used to study the dosimetric response of the detector, in the axial plane of the phantom, as a function of its angle with respect to the irradiation beam. A software has been developed to operate the rotation of this phantom and to acquire signals from the silicon strip detector. As an innovation, the detector was positioned inside the cylindrical phantom parallel to the beam axis. Irradiation experiments were carried out with a Siemens PRIMUS linac operating in the 6 MV photon mode at the Virgen Macarena Hospital. Monte Carlo simulations were performed using Geant4 toolkit and results were compared to Treatment Planning System (TPS) calculations for the absorbed dose-to-water case. Geant4 simulations were used to estimate the sensitivity of the detector in different experimental configurations, in relation to the absorbed dose in each strip. A final calibration of the detector in this clinical setup was obtained by comparing experimental data with TPS calculations.

1. Introduction

Radiation therapy is nowadays a well established technique in the treatment of tumors. As treatments are evolving and increasing in terms of complexity, a parallel development is required for dosimetric treatment verifications [1]. A common technique, although not simple, is the Intensity Modulated Radiation Therapy (IMRT) that uses a linac equipped with a multileaf collimator (MLC). The MLC incorporates tens of narrow, closely abutting tungsten leaves. Each leaf is individually motorized and controlled allowing the generation of irregular radiation fields. The desired absorbed dose distribution is obtained by irradiating the patient through many beam directions and entrance points, and by modulating in space the fluence of each radiation field [2,3].

Absorbed dose distribution verification is highly advisable prior to real dose delivery to the patient in complex radiotherapy treatments, as Treatment Planning Systems (TPSs) might miscalculate, under some circumstances, the dose delivered to the patient [4,5].

Ionization chambers for absolute point absorbed dose measurements and dedicated films for planar fluence verification are common devices and techniques used for quality assurance (QA) verification of treatment plans [2,6]. Film dosimetry is extensively accepted as 2D dosimeter [7] and there are many extensive reviews on it [8,9]. However, intrinsic measurement and reading processes make films unsuitable as *online* detectors. Therefore, it is necessary to develop new detection systems that enhance the traditional ones, and that are able to verify in a simple and accurate way complex treatment plannings. These detectors should also be inexpensive, radiation hard and easy to use.

* Correspondence to: National Accelerator Centre, C/Thomas Alva Edison, n.7 (Parque Tecnologico Cartuja 93), E-41092 Seville, Spain. Tel.: +34 954 460 553.
E-mail address: abocci@us.es (A. Bocci).

Digital devices based on 2D arrays are the best candidates to substitute film dosimetry [10]. Electronic portal imaging devices (EPIDs) and arrays based on either silicon detectors or ionization chambers are used as solutions for pre-treatment absorbed dose verification [11–14]. Such systems have the advantage over films that they can provide real-time measurements. However, the spatial resolution of commercial 2D arrays is still far from what is needed in treatment verification when compared to film dosimetry [15–17].

Many efforts have been done to develop silicon detectors for medical physics applications, taking advantage of the experience earned in detector technology from high energy physics research (i.e., on silicon tracking detectors and data acquisition systems) [18]. In particular, research is oriented towards silicon microstrip technology to improve spatial resolution in radiotherapy treatment verification [14,19,20]. Pixelated silicon array detectors were also developed, such as in the framework of the European project MAESTRO [21]. To obtain sub-millimetric spatial resolutions, these devices require a high number of allocated channels and a complex multichannel readout electronics based on application-specific integrated circuits (ASICs) [14,21–23].

These systems, however, are not ideal to obtain absorbed dose maps in axial planes. In fact, many of them are designed to be irradiated only perpendicularly with respect to detector's active area. This means that they are useful for the verification of each field, allowing to measure absorbed dose profiles but not full plan verification. Recently, a system based on diode crossed arrays in two perpendicular planes (Δ^4 by ScandiDos) has been developed [24,25]. However, the distance between two diodes is still large, 0.5 cm at the center of the boards and 1 cm at its periphery.

In this work, we present a feasibility study of a silicon strip detector to be used for obtaining absorbed dose maps in axial plane of a cylindrical phantom, to be applied to radiotherapy treatment verification. With the purpose of benchmarking this novel method, we have chosen a commercial, totally depleted, DC-coupled single-sided silicon strip detector (SSSSD), model W1(SS)-500 from Micron Semiconductor Ltd. [26]. This study comprises a calibration protocol, experimental measurements, data analysis and simulations used to validate this original technique. The work is organized as follows: in Section 2 we present the experimental setups and Geant4 simulations. In Section 3, measurements are reported and results on the characterization and angular response of the detector are discussed. In addition, comparisons with other methods, Geant4 simulations and TPS calculations, are also presented. Finally, conclusions are summarized in Section 4.

2. Materials and methods

2.1. Experimental setup: linac and phantoms

A Siemens PRIMUS™ linac dual energy machine operating in the 6 MV photon mode was used to test the detection system.

Since at therapy energies the interaction cross-section of photons with the phantom material is dominated by Compton scattering, non-local contributions of secondary electrons from primary photons interacting centimeters away, contribute to the absorbed dose. Two phantoms were designed to house the detector. The first one is a 30×30 cm^2 slab phantom made of polyethylene. Fig. 1 shows a picture of this experimental setup during a measurement. We can distinguish the linac, the slab phantom (with the detector inside) covered by several slices of solid water and the cable that connects the detector to the electronics.

Fig. 1. PRIMUS™ linear accelerator at the Virgen Macarena University Hospital in Seville and the experimental setup with the slab phantom mounted during a test.
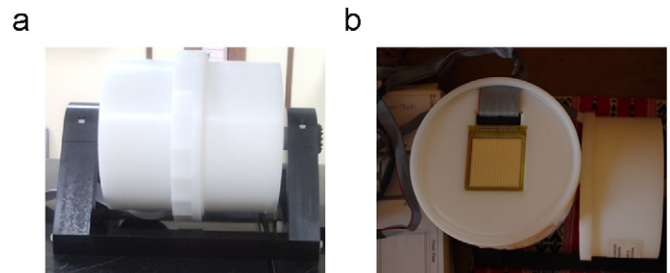

Fig. 2. (a) A picture of the cylindrical phantom. (b) Transverse section of the cylindrical phantom showing the detector in the axial plane.

In addition, since in clinical practice absorbed dose distributions are customarily displayed along axial planes, a cylindrical phantom made of polyethylene (diameter of 15 cm and height of 17 cm) was used to study the behavior of the detector when it is placed parallel to the beam axis (Figs. 2 and 3). Such phantom has the capability of rotating around its symmetry axis to study the angular response of the strip detector.

A software developed under LabVIEW platform permits to control the rotation of the cylindrical phantom using the RS232 communication protocol. There are two possibilities: selecting one fixed angle or moving automatically within a set of consecutive angles. Automatic operations are integrated in the overall treatment sequence for rotating the phantom during a full treatment.

2.2. Single-sided silicon strip detector

As commented previously, the detector used is a commercial, totally depleted, DC-coupled single-sided silicon strip detector (SSSSD) from Micron semiconductors Ltd., model W1(SS)-500 [26]. It is 500 μm thick and is divided into 16 strips, with 3.1 mm pitch, covering an active area of 50.0×50.0 mm^2. On the front face of n-type silicon wafer, the 16 strips consist of a region of heavily doped silicon by implantation of acceptor impurities to form a p$^+$ type material. An aluminum metalization with a thickness of 0.3 μm is applied on the junction side allowing good ultra sonic wire bonding connections. The silicon detector is mounted on a Printed Circuit Board (PCB) frame made out of FR4 material. The detector is connected to the readout electronics by a standard 16-conductor ribbon cable (2 m length) with an
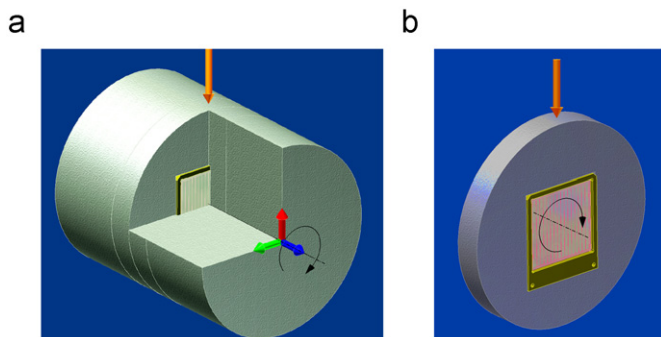
a

b

Fig. 3. (a) A scheme of the cylindrical phantom with the detector inserted in the axial plane. The vertical arrow represents the beam direction, parallel to the detector plane. The curved arrows represent the phantom rotation with respect to the beam. (b) The transverse section of the cylindrical phantom with the detector inside.
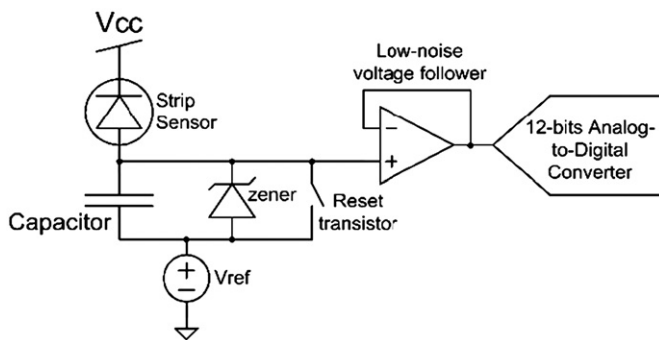
Fig. 4. A schematic view of the discrete front-end electronics.

insulated displacement connector. The $W1(SS)$ SSSSD design does not incorporate a guard-ring [26]. The detector was biased at 44 V and the measurements were performed at room temperature. This bias voltage was a good compromise between signal to noise ratio and sensitivity of the detector.

2.3. Electronics and software

The result of the incident irradiation on the silicon p–n diodes of the SSSSD is a weak current. Since we need to measure the total absorbed dose inside the material, the readout electronics is implemented as an electrometer, thus, integrating the total received charge. The front-end electronics is a conventional charge integrator. The output voltage, proportional to the charge, is digitized and analyzed using a digital signal processor (DSP). The signal is then digitally processed and transferred to a PC based application.

The schematic representation of the charge integrator for each channel is depicted in Fig. 4. Charge is collected using a low loss capacitor. The voltage across the capacitor, proportional to the amount of charge, is buffered to avoid charge losses. A 12-bit analog-to-digital (ADC) converter is used to digitize the voltage information. Since 16 strips must be monitored, two 8-channel converters are used. Each converter samples sequentially eight capacitor voltages. Phase delay from the different channels is negligible since the digital sampling frequency (above 1 kHz) is several orders of magnitude larger than the process maximum frequency (sub-Hertz). The maximum frequency is given by the bandwidth of the voltage waveform across the integrating capacitor. This voltage will increase proportionally to the absorbed dose. Since a measurement will consist in a constant irradiation over a given time period, the voltage will respond as a ramp signal with a Laplace transform given by $1/S^2$, where S is the Laplace

operator. Even if the response formally reaches higher frequencies, resolution and accuracy is not compromised if only sub-Hertz components are taken into account and sampled with the minimum frequency imposed by the Nyquist–Shannon sampling theorem [27]. Finally, both converters transmit the digital data via an Inter-Integrated Circuit serial protocol to the DSP.

A procedure for correcting offsets and gains, due to non-idealities of the electronic devices is performed during the data acquisition. Since each strip is connected to a different electronic chain, offset and gain compensations are calculated independently for each strip. Offset compensation is performed at the beginning of the measurements. A digitally controlled transistor (reset transistor) sets the integrating capacitor voltage to a reference value. This reference value is digitized and taken as the channel offset allowing to correct amplifiers and ADC offsets. During measurements, the obtained offset is subtracted to the sampling data. An uniformity factor is applied to each set of sampling data for correcting different efficiencies of the electronic chain. This factor depends on the circuital components, such as the integrating capacitor and is obtained by means of a dedicated measurement (see Section 3.3). Finally, a conversion factor is used by the DSP to convert the ADC output of each strip to the absorbed dose in Gy (see Section 3.4).

A software developed under *LabVIEW* platform [28] was used to retrieve data and to manage automatically the electrometer and the motor of the cylindrical phantom (Figs. 2 and 3). The data are transmitted via a *RS-232* serial bus. Standard communication parameters are used and speed was set to 9.600 baud rate. The sampling frequency of the read-out software is limited by data process during and after acquisition. DSP allows to reach sampling times lower than 100 ms, even if data acquisition is limited to a value of ∼ 700 ms due to DSP operations and to the software.

A PC receives from the DSP a set of values. These values are written in a data array for each sampling time of the electronics. Absorbed doses are plotted instantaneously versus the acquisition time on a graph. The plot is used to monitor the status of all strip doses during the treatment. Absorbed dose as a function of each strip is also shown on the main program interface. Data files present strip absorbed doses for each sampling time, at each rotation angle of the phantom, which allows a post-treatment analysis of data.

2.4. Geant4 simulations

The experimental setup was modeled with the Geant4 toolkit (*version 9.3.p01*) [29,30]. The geometry of the Siemens PRIMUS™ treatment head, operating in the 6 MV nominal energy photons, was reproduced in detail according to the manufacturer's specifications concerning target, flattening filter, monitor chamber, jaws and the multi-leaf collimator [31]. The geometric model of the phantoms was built according to our design layouts (including the air gaps and lateral supports) [32]. The SSSSD was reproduced following the specifications given by the manufacturer [26].

The physics list was defined using the *Livermore Low-Energy Electromagnetic* processes implemented in Geant4 [33], which describes the interaction with matter of electrons and photons at kinetic energies down to 250 eV. Cross-sections are calculated by means of the evaluated data libraries *EPDL97* [34], *EEDL* [35] and *EADL* [36] for photons, electrons and atomic relaxations, respectively. The electromagnetic interactions of the other particles were simulated with the *Standard Electromagnetic* package [37]. Hadronic interactions were not considered in the 6 MV photon mode of the Linac. Production cuts were set to 50 μm in the entire setup.

The goal of these simulations was to estimate the sensitivity of the SSSSD in different experimental situations based on the absorbed dose in each strip. Thus, an energy deposition "scorer" was registered for each strip of the SSSSD (Section 3.8.2). The Geant4 results were compared with the experimental measurements and to the calculations obtained with the TPS.

3. Measurements and results

First of all the detector was hosted inside the slab phantom and was irradiated with the beam axis perpendicular to its active area (Fig. 1). This setup was used to characterize the detector and to perform a first calibration in absorbed dose following standard procedures. After this characterization the detector was placed inside the cylindrical phantom for studying its behavior in a plane parallel to the beam axis as a function of its angular position with respect to the symmetry axis of the cylinder (Fig. 2). The measurements performed with this arrangement yield a new calibration of the detector positioned with the same layout to be used in treatment verification. A schematic description of these measurements is shown in Fig. 3. All the measurements presented were performed with a dose rate of 200 Monitor Units (MU) per minute. A single MU is the amount of charge measured by the internal ionization chamber of the linear accelerator, which correlates with an absorbed dose of 0.01 Gy delivered to a water phantom under reference conditions. The reference condition is characterized by a radiation field of $10 \times 10 \, cm^2$, a source-to-surface distance (SSD) equal to 100 cm and the detector placed at a depth of 1.5 cm of water slabs. In this configuration the absorbed dose in Gy, in the center of the beam axis, is equal to the number of MU delivered by the linac.

3.1. Linearity

One of the main desired characteristics of a detector for dosimetric measurements is a linear response with the absorbed dose [2,3]. The study of the detector linearity was performed using the raw signal (i.e. before the uniformity, efficiency corrections and calibration) at the output of the ADC for each electronic channel (i.e. each detector strip). This signal was registered as a function of irradiation of the detector under the following conditions: SSD equal to 100 cm and detector placed at a depth of 2 cm of water slabs, $10 \times 10 \, cm^2$ radiation field, irradiating the device up to 500 MU while registering the output absorbed dose. As an example, the data of one single strip (number 11) represented with open circles and the linear fit represented with a solid line are shown in Fig. 5. The adjusted R^2 is 0.99997. The deviation from linearity of the absorbed dose signal in the range between 0.04 Gy and 5 Gy is of order of 0.1%. For all the strips the percentage of non-linearity is remarkably low, always within 0.1% deviation.

3.2. Reproducibility

In order to study the reproducibility of strip signals, the detector was irradiated six times with a constant number of MU, under reference condition. All the strips, at different absorbed dose measurements, present a reproducibility better than 0.5%.

3.3. Uniformity

Dedicated measurements for correcting the channel to channel variation of the 16 strips were performed. These measurements were necessary since each strip of the detector and each
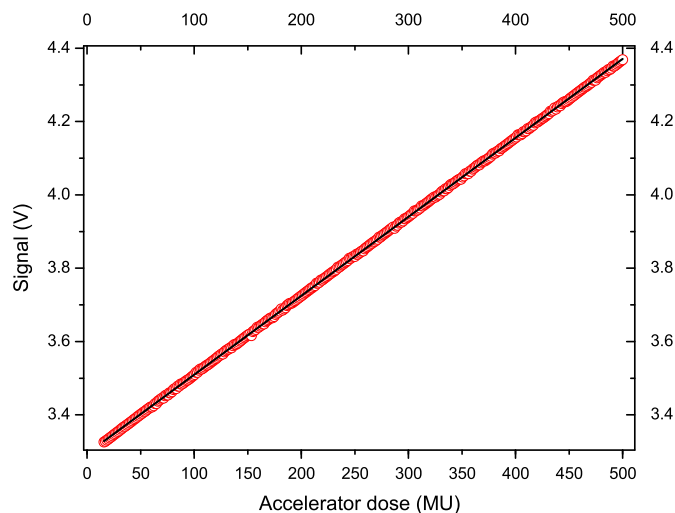

Fig. 5. Measurement of the linearity of one single strip (number 11) reported with open circles as a function of the accelerator dose delivered by the accelerator (500 MU). Solid line represents a linear fit of data.

electronic chain has a slightly different response, due to different connections, capacitances, amplifications, etc.

The response of the electronic chain was studied by irradiating the detector with a standard flat field of $10 \times 10 \, cm^2$, larger than the detector dimensions (active area of $5 \times 5 \, cm^2$). The experimental configuration was: source to surface distance SSD=90 cm at 10 cm of water depth. In this configuration the variations of the absorbed dose measured by a single channel silicon diode was within 1%.

In order to calculate the correction factor F for each channel i, the signal X_i was divided by the average signal $\langle X \rangle$ of strips 2–15. Strips 1 and 16 had a non-reproducible behavior, which is attributed to the edge effects of the device (the PCB board material) and to the lack of a guard-ring in the silicon strip detector [26]. The guard ring in fact minimizes the edge effects guaranteeing an homogeneous electric field in the active detection volume [38].

Factors F_i, obtained with three different measurements, were used to correct the channel to channel variations. The corrected signal X_i^c of each strip is calculated by dividing the measured signal X_i^m by each factor F_i

$$X_i^c = X_i^m / F_i. \tag{1}$$

Signals of each strip, normalized to the average signal of all strips, are shown in Fig. 6. One measurement with the raw detector response is shown with open circles, and the result after correcting by the uniformity factors F_i is shown with filled circles. The error bars of raw measurements reported are due to the instrumental precision of our system of 6.6 mGy. The errors of corrected measurements reported are only due to statistical deviations (1σ) of the F_i factors over three irradiations. The complete error treatment is depicted in Section 3.5.

Variations between all channels (strips), before applying the uniformity correction, were within 2%. After performing the uniformity correction, the channel-to-channel variations were below 0.5% (filled circles in Fig. 6).

Using this procedure, a preliminary uniformity correction of the detector was performed. All following data were corrected by uniformity factors.

3.4. Absorbed dose calibration

After the uniformity measurements, a conversion of the output voltage of the detector to the absorbed dose in Gy was obtained.
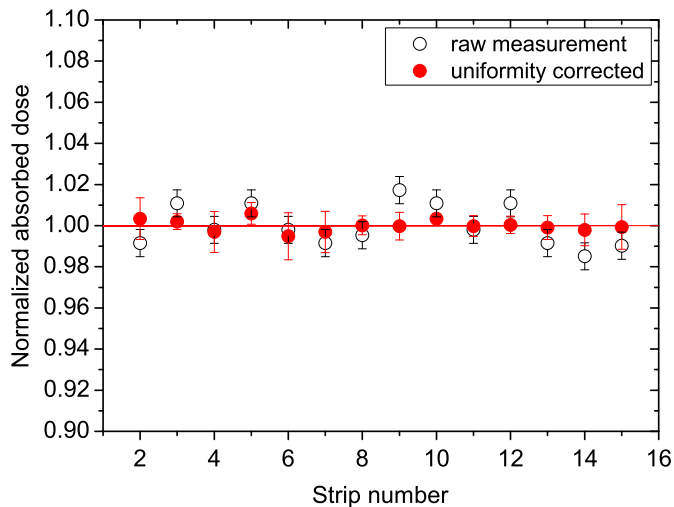
Fig. 6. The raw measurement of the detector response normalized to the average signal of all strips obtained with a flat field is reported with open circles. The corrected response obtained from the uniformity factors is shown with filled circles.
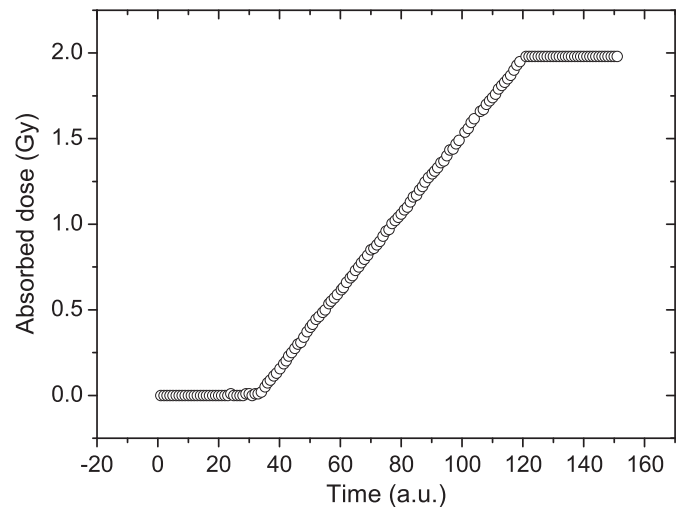

Fig. 7. Calibrated signal of the central strip (number 8) acquired during the irradiation and used to convert the delivered dose of the accelerator from MU to the absorbed dose in Gy.

In order to perform this conversion, the detector housed inside the slab phantom was irradiated with 200 MU under reference conditions. The dose delivered by the accelerator at the center of the beam was previously calibrated by an ionization chamber, traceable to the Spanish Nuclear National Laboratory. The calibration was obtained using the mean signal of central strips (8 and 9) to convert 200 MU into an absorbed dose of 2 Gy. In order to perform this conversion, an individual gain was set by the DSP to each strip channel with respect to the two central strips using this relation: $D_i = S_i \cdot 2\,\text{Gy}/\langle S \rangle$, where D is the calibrated absorbed dose to water for each strip i, $\langle S \rangle$ is the mean signal of the two central strips (8 and 9) and S_i is the signal of each strip obtained during a measurement.

As an example, the signal of strip number 8 after the calibration, as a function of the sampling time during irradiation, is represented in Fig. 7: in the first part of the measurement, the background level (set to zero by the DSP) is visible before starting the irradiation; the second part of the curve shows the linearity of the signal during dose delivery and finally the third part shows the constant value of the final absorbed dose after stopping the irradiation.

3.5. Error treatment

Due to the limited range of the ADC converter (12 bits), the minimum absorbed dose detected by our system was of 13.2 mGy, for a dynamic range of 54 Gy. This value was chosen after programming the electronics in order to have a good compromise between the dynamic range of the ADC and its linearity. Since the electronics work as an electrometer, for each measurement the final value of the signal at the end of the irradiation was taken as the absorbed dose (see Fig. 7). The uncertainty associated to the measurement due to the quantization error of the ADC was: $\sigma_{X_i} = 1/2\,\text{LSB} = 6.6\,\text{mGy}$, where LSB is the less significative bit of the ADC [39], equal to 13.2 mGy.

The uncertainty of the whole system was calculated propagating the uncertainties of the independent variables in Eq. (1) for each strip signal X_i^m

$$\sigma_{X_i^c} = (\sigma_{X_i^m}/X_i^m + \sigma_{F_i}/F_i) \cdot X_i^c, \tag{2}$$

where σ_{F_i} is the experimental standard deviation of the uniformity correction factors for each strip i and $\sigma_{X_i^m}$ is the uncertainty
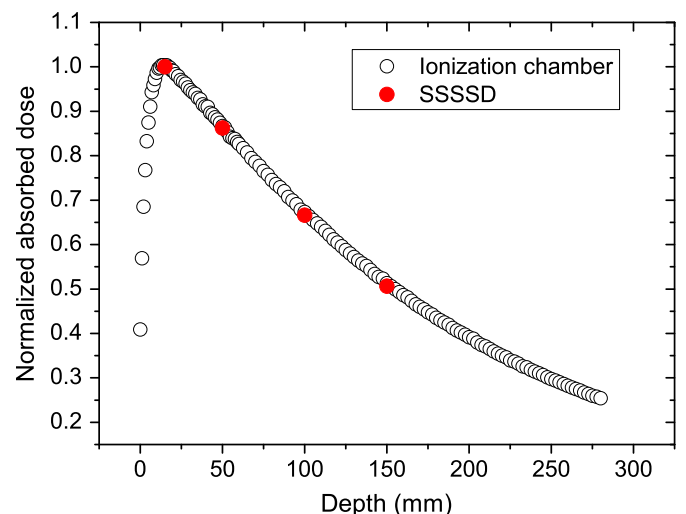

Fig. 8. Depth dose curve (normalized to 1) measured with the SSSSD is reported with filled circles and compared to the measurements performed with the ionization chamber (open circles).

associated to the measurement due to the quantization error of the ADC. For an absorbed dose of 2 Gy, the relative uncertainty (1σ) is smaller than 1.4%.

3.6. Percent depth dose

To study the percent depth dose (PDD), the detector was housed inside the slab phantom at SSD=100 cm. A field of $10 \times 10\,\text{cm}^2$ was used to irradiate the device with 200 MU and several slabs of water were used to measure the percent depth dose at the following depths: 1.5 cm, 5 cm, 10 cm and 15 cm. Fig. 8 shows the PDD measured by the SSSSD compared to the data of the ionization chamber. SSSSD data taken from central strips were normalized with respect to the one obtained at 1.5 cm from the ionization chamber. In Fig. 8, measurements of the SSSSD are represented with filled circles and data of the ionization chamber with open circles. The agreement between both data is very good. The difference is 0.68% at 10 cm and 0.73% at 15 cm of depth. In all cases, the statistical errors (1σ) of the SSSSD measurements with respect to the ionization chamber are smaller than 1%.

3.7. Penumbra

We define the penumbra size of the treatment field as the region between 20% and 80% of the maximum absorbed dose levels at 1.5 cm water depth. The experimental setup was obtained by blocking half part of the radiation field, defining a field of 5×10 cm^2 with the MLC.

Experimental data of the SSSSD and Geant4 simulations modeling the detector are reported in Fig. 9 with open and filled circles, respectively. These data were compared to a measurement obtained with a one-channel silicon detector (*Scanditronix* p-Si detector) and to Geant4 simulations in a water tank, reported with open and filled squares, respectively. The one-channel silicon detector has a diameter of 2.5 mm and the measurements were obtained by moving the detector with steps of 1 mm. Geant4 simulations in a water tank (absorbed dose-to-water) were calculated with a voxel size of 50 mm^3.

The penumbra obtained by the SSSSD and with the Geant4 simulation modeling the detector (SSSSD case) was 6.17 ± 0.56 mm and 5.58 ± 0.25 mm, respectively. The penumbra obtained by the single channel silicon detector was 3.92 ± 0.20 mm. Finally, penumbra calculated with Geant4 in a water tank (absorbed dose-to-water) gave a value 3.84 ± 0.25 mm.

SSSSD data and Geant4 simulations (SSSSD case) are compatible within uncertainties. Data obtained with the one-channel silicon detector and with Geant4 (absorbed dose-to-water) are also compatible. However, SSSSD data gave a penumbra value larger than the one obtained when using the one-channel silicon detector and this effect is clearly visible in Fig. 9. This approximately 1.5 times larger penumbra for the SSSSD with respect to the one channel silicon detector is attributed to its strip pitch of 3.1 mm.

3.8. Angular response measurements

Since the most common way to present absorbed dose distributions in radiotherapy is a 2D absorbed dose map in the axial plane of the patient, we have placed the detector inside the cylindrical phantom parallel to the beam axis (see Fig. 2(a) and (b)).
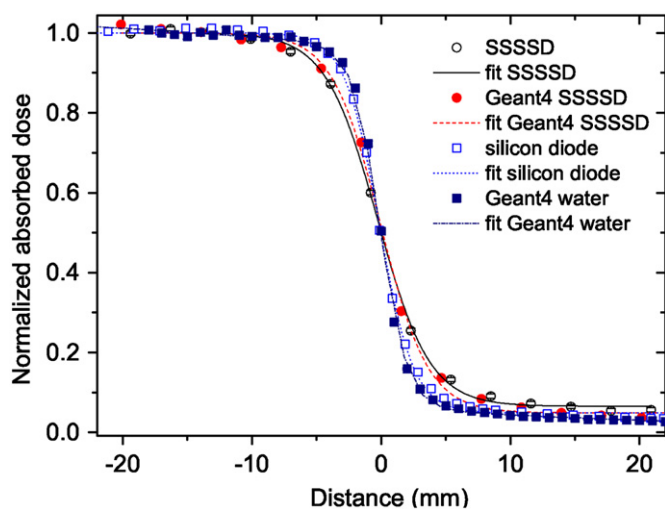
A set of measurements was performed varying the gantry angle and rotating the phantom (see Fig. 3). This provided also a measurement of the uncertainties of the phantom rotation with respect to the accelerator gantry angles.

The center of the detector, located on the rotation axis of the phantom, was positioned at the isocenter of the accelerator, located at 100 cm from the source. Each shot consisted of 200 MU, using a 10×10 cm^2 radiation field. As a reference, gantry and phantom angles equal to 0° correspond to the configuration in which all strips are parallel to the beam direction (vertical irradiation). The measurements were carried out by rotating the gantry at an angle θ, which value was from 0° to 315°, with a step of 45° leaving the detector fixed at 0°. Another set of measurements was obtained by fixing the gantry at 0° and rotating the phantom, in the same direction as the gantry from 0° to 315°, with a step of 45°. The measurements obtained by rotating the gantry at an angle θ were compared to the ones obtained by rotating the phantom at (360°-θ). In these configurations the irradiation is symmetric so the two measurements are equivalent and can be compared.

In Fig. 10 the absorbed dose in each strip is shown at different irradiation angles. For each measurement, the value of the gantry rotation angle, θ, is reported on the top of each panel. The experimental data obtained rotating the gantry and phantom are represented with filled and open circles, respectively. The error bars reported in Fig. 10 were calculated considering the experimental uncertainties discussed in Section 3.5.

Fig. 10 shows a total compatibility between both experimental data described above. The agreement is also remarkable, considering the presence of errors due to the misalignment of the phantom with respect to the beam during the measurements.

3.8.1. TPS calculations

A Computed Tomography (CT) image of the system in the transverse plane was performed (see Fig. 11) in order to calculate the absorbed dose of each strip with the TPS. In the CT scan of
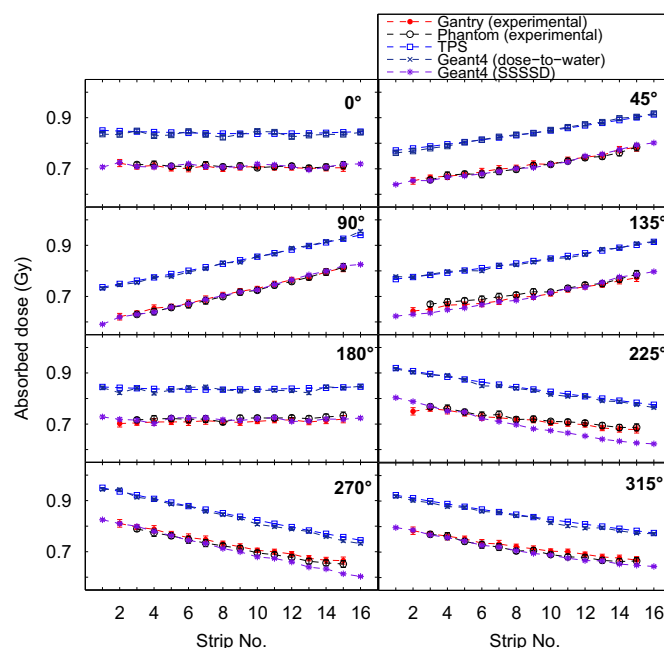

Fig. 9. Penumbra measured under reference conditions. The SSSSD data and Geant4 simulations (SSSSD case) are reported with open and filled circles, respectively. The measurements obtained with one channel silicon detector and Geant4 (absorbed dose-to-water) are shown with open and filled squares. The curve fits used to calculate the penumbra for the SSSSD and Geant4 (SSSSD case) are reported with a solid and a dashed line, respectively. The curve fits of the one channel silicon detector and Geant4 (absorbed dose-to-water) are shown with dot and dash-dot lines.

Fig. 10. Absorbed doses as a function of the strip number for each angle θ of irradiation. Experimental data rotating the gantry and phantom are reported with filled and open circles, respectively. TPS data are reported with open squares. Geant4 simulations (absorbed dose-to-water case) and Geant4 (SSSSD case) are reported with cross- and star-symbols, respectively.
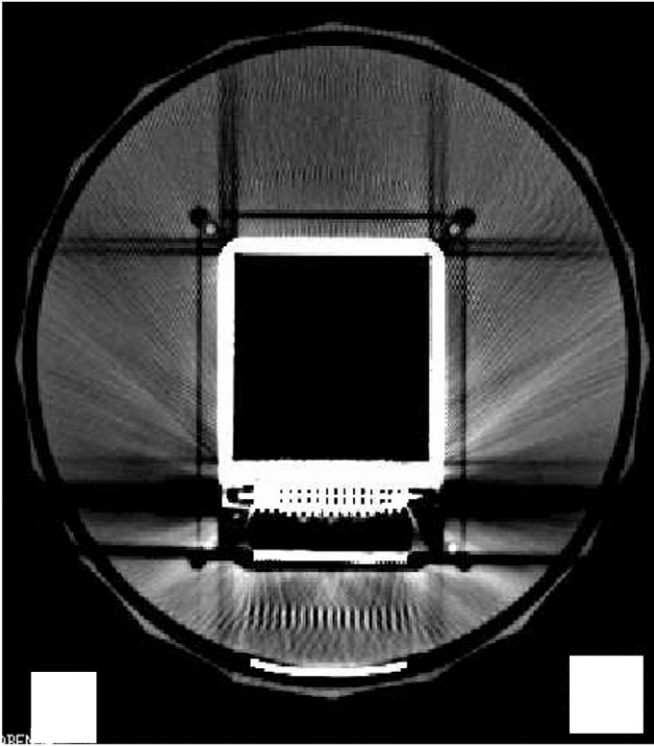
Fig. 11. CT scan in the transverse plane of the cylindrical phantom. The CT image shows the active area of the SSSSD, the PCB board, the connector, the cable and the cylindrical phantom.

Fig. 11, the active area of the detector (the black square area at its center), the PCB board (the white edge that delimits the detector area), the connector, the cable and the cylindrical phantom can be clearly distinguished. The CT image was used to divide the active area of the device into 16 strips. Then the absorbed dose in each strip was calculated with the TPS (Philips Pinnacle[3]) with the gantry at $\theta = 0°$ and finally, this absorbed dose map was rotated to obtain the absorbed dose for each strip at the rotation angles reported previously. In the TPS calculation we assumed that the entire phantom, including the detector, was water, so only absorbed dose-to-water values were calculated. The estimated uncertainty of the TPS calculation was 1 mGy. Calculated absorbed doses using the TPS are reported in Fig. 10 with open squares.

3.8.2. Geant4 simulations

Geant4 simulations were performed both to estimate the absorbed dose-to-water data and the actual absorbed dose in the SSSSD strips. In both cases, the cylindrical phantom and the SSSSD were modeled with sub-millimetric detail. In the first case, both phantom and detector were assumed to be made of water. In the second case, the actual materials were used, the gantry angle was set to $\theta = 0°$ (vertical irradiation) and the cylindrical phantom was rotated to different angles in order to obtain the different orientations of the detector strips with respect to the beam.

Geant4 simulation for the absorbed dose-to-water case is reported in Fig. 10 with cross-symbols. The results are fully compatible within uncertainties with the TPS calculations. The relative difference between these data is smaller than 1.7% for all the strips at different angle orientations. Error bars (1σ) of Geant4 simulations are about 0.8%.

The absorbed dose values calculated with Geant4 considering the actual materials are also shown in Fig. 10 with star symbols.

The Monte Carlo calculations are compatible with the experimental data measured with the SSSSD. Small differences are due to the alignment and to the errors in the angle of rotation of the detector inside the cylindrical phantom. In Fig. 10 the agreement between the tendency of Geant4 calculation at different angles (SSSSD case) and the TPS is also noticeable. This implies that a new calibration factor will be independent from the irradiation angle. In the next Section 3.8.3 a deeper discussion is presented.

3.8.3. Comparison between experimental data and TPS

Fig. 10 shows differences of about 14% between calculations obtained using the TPS and the SSSSD data. These differences are due to the dissimilar orientations of the detector: in the cylindrical phantom (parallel configuration) and in the slab phantom (perpendicular configuration), in which the absorbed dose calibration was obtained (Section 3.4). Consequently a new calibration factor is necessary for the parallel configuration, that, based on Fig. 10, seems to be constant.

In order to study this new calibration factor quantitatively and to investigate its dependence with respect to the strip number i and to its irradiation angle θ, the ratios $R_i(\theta)$ between SSSSD absorbed doses D_i and TPS absorbed doses D_i^{TPS} were calculated for each strip

$$R_i(\theta) = D_i(\theta)/D_i^{TPS}(\theta). \tag{3}$$

The values of $R_i(\theta)$ are plotted in Fig. 12 with open circles at different angles θ for each strip, reported on the top of each panel. For the SSSSD data, the mean of the two measurements (gantry and phantom rotations) for each angle was used to calculate $R_i(\theta)$.

As commented before, Fig. 12 shows that the ratio between experimental data and TPS at different angles is constant within error bars. A constant fit of each strip data is reported with solid lines. The error bars taken from the constant fits represent the 95% confidence interval of the best-fits (2σ deviation). From these results, for each strip we found a calibration factor $R_i(\theta)$ independent of the irradiation angle $R_i(\theta) \approx R_i$. The non-dependence on the irradiation angles with respect to the strips is a remarkable result that simplifies outstandingly the detector calibration.
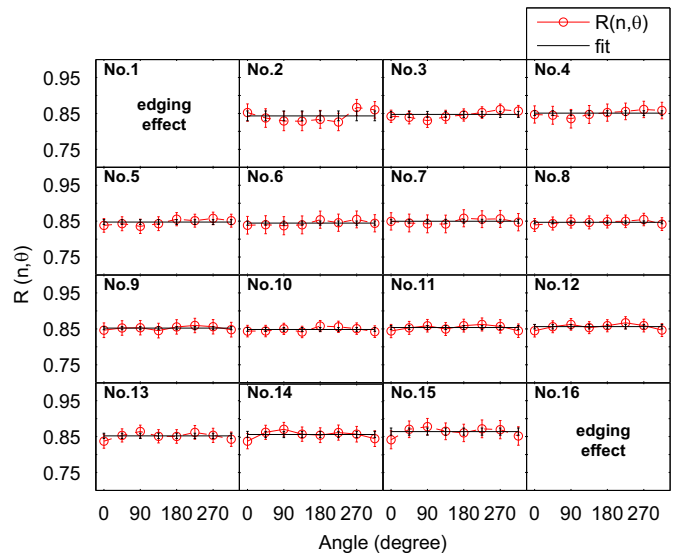

Fig. 12. Ratio between SSSSD data and TPS calculations with respect to the irradiation angle is reported with open circles (see Eq. (3)). Fits of the constant functions and error bars are shown with solid lines. Strip numbers of measurements are reported on the top of each panel.
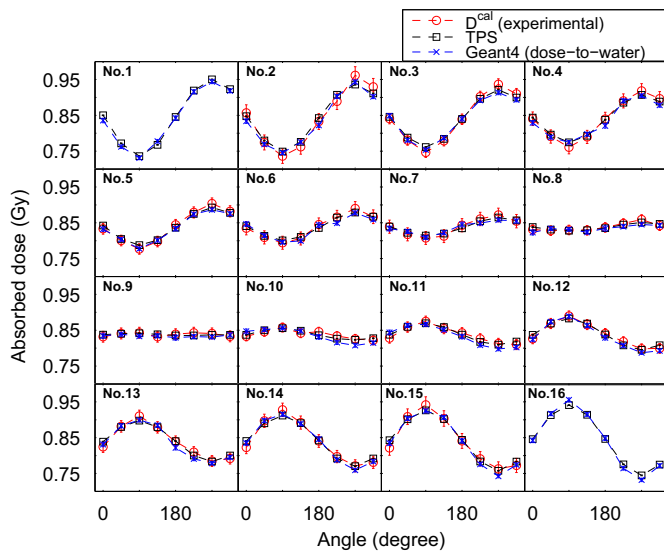
Fig. 13. Calibrated absorbed doses of the SSSSD calculated using Eq. (4) are reported with open circles and compared to TPS calculations, reported with open squares. Geant4 simulations (absorbed dose-to-water) are shown also with cross-symbols.

3.8.4. Final calibration

The absorbed dose calibrated with respect to the TPS, D^{cal}, were calculated by dividing the measured absorbed dose D_i by the R_i factors

$$D_i^{cal} = D_i/R_i. \tag{4}$$

Fig. 13 shows the values of D_i^{cal} obtained with the SSSSD and compared with the TPS calculations and Geant4 simulations (absorbed dose-to-water case). Calibrated absorbed doses are reported with open circles, TPS calculations and Geant4 simulations with open squares and cross-symbols, respectively. Error bars from experimental data were calculated propagating the uncertainties of the independent variables in Eqs. (3) and (4). Fig. 13 shows the good agreement between calibrated absorbed dose, TPS calculations and Geant4 (absorbed dose-to-water). The relative difference between the calibrated absorbed dose and TPS calculations was found better than 2% for the strips at the edges of the SSSSD, and even better than 1% for the central ones (see Fig. 13).

4. Conclusions

This work is part of a more ambitious project aiming to benchmark a prototype based on a Si strip detector. The final goal of the project is to employ this prototype for obtaining 2D dose maps by means of an in-house developed algorithm (patent pending), dedicated to verify complex radiotherapy treatment plans.

In order to achieve this objective, an experimental setup was designed, built and tested. This setup includes two polyethylene phantoms. The first one is a slab phantom dedicated to study the dosimetric behavior of the detector. The second one is a cylindrical phantom capable of rotating around its symmetry axis, built for studying the angular response of the detector and for 2D absorbed dose verification plan. This setup has the capability of measuring absorbed dose maps in a plane parallel to the beam axis (axial plane). This condition is close to the one normally used in clinical environments. This is the most important advantage of this system in comparison with other methods based on 2D arrays used for radiotherapy quality assurance (QA). In fact, most

of these devices allow the measurement of the absorbed dose map only in the coronal plane.

As an inexpensive solution to validate the novel technique proposed, we chose a commercial single-sided silicon strip detector (SSSSD) divided into 16 strips, to be irradiated with a Siemens PRIMUS linac operating in the 6 MV photon mode. The characterization of the SSSSD showed that the prototype has the necessary characteristics to be adopted in QA verification plans. The linearity of all the strips is better than 0.1% and the corrected uniformity is within 0.5%. The reproducibility was within 0.5%. PDD results are compatible within 1% with respect to values measured with an ionization chamber. Penumbra resulted with a factor of 1.5 larger than the value obtained using a one channel silicon detector, due mostly to the large strip pitch of the SSSSD (3.1 mm). The total uncertainties of our system were estimated to be smaller than 1.4% (1σ) for an absorbed dose of 2 Gy.

Monte Carlo simulations of the experimental setup were performed using the Geant4 toolkit. Both phantoms were modeled including the SSSSD as well. Results of SSSSD simulations showed a good agreement with respect to experimental measurements for the characterization of the detector, performed with the slab phantom. Simulations of cylindrical phantom gave results compatible with the absorbed dose-to-water TPS calculations and with the detector measurements. Monte Carlo simulations turned out to be a very powerful tool for the characterization of such prototype and to check the suitability of the experimental setup.

The angular dependence of the detector was studied and compared to TPS calculations. We found that the response of the detector was independent from the irradiation angle. Finally, each strip was calibrated with respect to the absorbed dose-to-water calculations of the TPS. After this calibration, differences between data and TPS were smaller than 2% for the strips at the edges of the SSSSD, and even better than 1% for the central ones. However a better spatial resolution must be obtained by using a SSSSD with a smaller strip pitch and more channels, or by using a pixelated silicon detector. Because of the higher number of channels, improvements in the performance of the setup should be reached using a dedicated electronics based on ASIC's.

References

[1] C.D. Wagter, Journal of Physics: Conference Series 3 (2004) 4.
[2] E.B. Podgorsak (Ed.), Radiation Oncology Physics: A Handbook for Teachers and Students, IAEA, 2005. Available online from w?w?w?.iaea.org.
[3] IMRT Collaborative Working Group, International Journal of Radiation Oncology Biology Physics 51 (2001) 880.
[4] J. Dyk, R. Barnett, J. Cygler, P. Shragge, International Journal of Radiation Oncology, Biology, Physics 26 (1993) 261.
[5] P. Cadman, R. Bassalow, N. Sidhu, G. Ibbott, A. Nelson, Physics in Medicine and Biology 47 (2002) 3001.
[6] M. Bucciolini, F.B. Buonamici, M. Casati, Medical Physics 31 (2004) 161.
[7] O.A. Zeidan, S.A.L. Stephenson, S.L. Meeks, T.H. Wagner, T.R. Willoughby, P.A. Kupelian, K.M. Langen, Medical Physics 33 (2006) 4064.
[8] A.N.-R. Chair, C.R. Blackwell, B.M. Coursey, K.P. Gall, J.M. Galvin, W.L. McLaughlin, A.S. Meigooni, R. Nath, J.E. Rodgers, C.G. Soares, Medical Physics 25 (1998) 2093.
[9] R. Arrans, H. Miras, M. Ortiz-Seidel, J. Terrón, M.J.A. Ortiz-Lora, Revista de Física Médica 2 (2009) 83.
[10] ⟨http://www.aapm.org/meetings/05AM/pdf/18-4147-88232-65.pdf⟩.

[11] C. Talamonti, M. Casati, M. Bucciolini, Medical Physics 33 (2006) 4367.
[12] A.B. Rosenfeld, Radiation Measurements 41 (2006) S134.
[13] P.A. Jursinic, B.E. Nelms, Medical Physics 30 (2003) 870.
[14] J.H.D. Wong, M. Carolan, M.L.F. Lerch, M. Petasecca, S. Khanna, V.L. Perevertaylo, P. Metcalfe, A.B. Rosenfeld, Medical Physics 37 (2010) 427.
[15] F. Banci Buonamici, et al., Medical Physics 34 (2007) 1372.
[16] J. Li, G. Yan, C. Liu, Journal of Applied Clinical Medical Physics 10 (2009) 62.
[17] S. Saminathan, R. Manickam, V. Chandraraj, S. Supe, Journal of Applied Clinical Medical Physics 11 (2010).
[18] R. Ballabriga, M. Campbell, E. Heijne, X. Llopart, L. Tlustos, W. Wong, Nuclear Instruments and Methods in Physics Research Section A: Accelerators, Spectrometers, Detectors and Associated Equipment, 633, Supplement 1, (2011) S15.
[19] I. Redondo-Fernandez, C. Buttar, S. Walsh, S. Manolopoulos, J. Homer, S. Young, J. Conway, Nuclear Instruments and Methods in Physics Research Section A: Accelerators, Spectrometers, Detectors and Associated Equipment 573 (2007) 141.
[20] A.J. Cullen, Master's Thesis, Centre for Medical Radiation Physics, Faculty of Engineering, University of Wollongong, 2009.
[21] C. Talamonti, M. Bruzzi, M. Bucciolini, L. Marrazzo, D. Menichelli, Nuclear Instruments and Methods in Physics Research Section A: Accelerators, Spectrometers, Detectors and Associated Equipment 583 (2007) 114.
[22] S. Manolopoulos, C. Wojnecki, R. Hugtenburg, M.A.J. Sidek, G. Chalmers, G. Heyes, S. Green, Physics in Medicine and Biology 54 (2009) 485.
[23] D. Menichelli, M. Bruzzi, M. Bucciolini, C. Talamonti, M. Casati, L. Marrazzo, M. Tesi, C. Piemonte, A. Pozza, N. Zorzi, M. Brianzi, A. De Sio, Nuclear Instruments and Methods in Physics Research Section A: Accelerators, Spectrometers, Detectors and Associated Equipment 583 (2007) 109.
[24] J.L. Bedford, Y.K. Lee, P. Wai, C.P. South, A.P. Warrington, Physics in Medicine and Biology 54 (2009) N167.
[25] R. Sadagopan, J.A. Bencomo, R. Landrove Martin, G. Nilsson, T. Matzen, P. Balter, Journal of Applied Clinical Medical Physics 10 (2) (2009) 2928.
[26] ⟨http://www.micronsemiconductor.co.uk/⟩.
[27] C. Shannon, Proceedings of the IRE 37 (1949) 10.
[28] ⟨http://www.ni.com/labview/⟩.
[29] S. Agostinelli, et al., Nuclear Instruments and Methods in Physics Research Section A: Accelerators, Spectrometers, Detectors and Associated Equipment 506 (2003) 250.
[30] J. Allison, et al., IEEE Transactions on Nuclear Science NS-53 (2006) 270.
[31] M.A. Cortes-Giraldo, J.M. Quesada, M.I. Gallardo, AIP Conference Proceedings, vol. 1231, 2010, p. 209.
[32] M.A. Cortes-Giraldo, M.I. Gallardo, R. Arrans, J.M. Quesada, A. Bocci, J.M. Espino, Z. Abou-Haidar, M.A.G. Alvarez, Progress in Nuclear Science and Technology 2 (2011) 191.
[33] S. Chauvie, S. Guatelli, V. Ivanchenko, F. Longo, F. Mantero, B. Mascialino, P. Nieminen, L. Pandola, S. Parlati, L. Peralta, M.G. Pia, M. Piergentili, P. Rodrigues, S.S.A. Trindale, Nuclear Science Symposium Conference Record, 2004, vol. 3, IEEE, 2004, p. 1881.
[34] D.E. Cullen, J.H. Hubbell, L. Kissel, EPDL97: the evaluated photon data library, '97 version, Report UCRL-50400, Lawrence Livermore National Laboratory, 1991.
[35] S.T. Perkins, D.E. Cullen, S.M. Seltzer, Tables and graphs of electron-interaction cross-sections from 10 eV to 100 GeV derived from the LLNL evaluated electron data library (EEDL), Z=1–100, Report UCRL-50400, Lawrence Livermore National Laboratory, 1991.
[36] S.T. Perkins, D.E. Cullen, M.H. Chen, J.H. Hubbell, J. Rathkopf, J. Scofield, Tables and graphs of atomic subshell and relaxation data derived from the LLNL evaluated atom data library (EADL), Z=1–100, Report UCRL-50400, Lawrence Livermore National Laboratory, 1991.
[37] H. Burkhardt, V.M. Grichine, P. Gumplinger, V.N. Ivanchenko, R.P. Kokoulin, M. Maire, L. Urban, in: Proceedings MC2005, American Nuclear Society, LaGrange Park, IL, Chattanooga, Tennessee, April 17–21, 2005.
[38] F. Hartmann, Evolution of Silicon Sensor Technology in Particle Physics, Springer-Verlag, 2009.
[39] G. D'Antona, A. Ferrero, Digital Signal Processing for Measurement Systems: Theory and Applications Reference, Springer, 2005.